# Density Functional Theory Study of the Structure of the Pillared Hofmann compound Ni(3-Methy-4,4'-bipyridine)[$Ni(CN)_4$] (Ni-BpyMe or PICNIC-21)

Eric Cockayne[1*], Winnie Wong-Ng[1], Yu-Sheng Chen[2], Jeffrey T. Culp[3], Andrew J. Allen[1]

[1]Materials Measurement Science Division, Material Measurement Laboratory, National Institute of Standards and Technology, 100 Bureau Dr., Gaithersburg, MD 20899-8520 USA,

[2]ChemMatCARS, University of Chicago, Argonne, IL 60439.

[3]LRST/Battelle, National Energy Technology Laboratory, United States Department of Energy, P.O. Box 10940, Pittsburgh, PA 15236

*Email: eric.cockayne@nist.gov; Telephone (1) 301-975-4347

**Abstract**

We use dispersion-corrected density functional theory (DFT) to investigate the structure of the pillared Hofmann compound Ni(3-Methy-4,4'-bipyridine)[$Ni(CN)_4$] (Ni-BpyMe for short, or PICNIC-21). We model the disorder found in experimental X-ray structure refinement via an ensemble of supercells with ordered ligand orientation configurations. The ensemble-averaged structure agrees very well with experiment, except for the positions of the methyl group hydrogen atoms. While the dihedral angles between the bipyridal rings of each BpyMe ligand of the averaged structure is 90°, the local dihedral angles are about 80°. DFT screening of configurations where the crystallographic a/b ratio is constrained to equal 1 fail to find the configurations that are most stable when a/b is set to its distorted experimental value of a/b = 0.86, demonstrating the difficulty of solving pillared Hofmann structures purely theoretically without experimental input. The waviness of the $Ni(CN)_2$ sheets is explained as a tendency to maximize dispersion interactions between these sheets and the methyl pyridine rings. This waviness leads to greater residual pore space and greater adsorbate uptake at low pressure compared with the analogous pillared compound Ni-Bpene (PICNIC-60).

**Introduction**

Metal-organic frameworks (MOFs) are a class of materials where metal ions or clusters are linked by coordinated organic ligands into a three-dimensional network, typically with high porosity. (1-5) Their crystalline microporosity makes MOFs candidates for applications in gas storage and separation. (6-10) The ability to engineer the structure and properties of MOFs by changing the metal species, ligands, topology, etc., make them a continued subject of very active research.

A subclass of MOFs is the family of flexible metal-organic frameworks. (11-15) In these MOFs, the structure can expand from a small-pore to a large-pore structure, often without change in the topology of the metal-ligand network. In one case, of MIL-88 (Ref. 16), the volume expands by a factor of nearly 2 between these phases. External stimuli such as pressure and temperature, can cause the transition between the two phases when their free energy difference is small (17), making flexible MOFs intriguing candidates for gas adsorption materials whose adsorption and desorption is based on swings in temperature, pressure, etc.

A family of microporous compounds related to MOFs is the pillared cyanonickelate ("PICNIC") family (18). PICNIC compounds are based on square planar sheets of $Ni(CN)_2$ bridged by organic ligands terminated by N on each end. The $Ni(CN)_2$ sheets have an ordered arrangement of the cyanide units such that alternating Ni are N and C coordinated. In most PICNIC structures, the N-coordinated Ni are also coordinated by the N of an organic ligand both above and below, leading to 6-fold N coordination of these Ni and an extended three-dimensional structure. In the idealized case with perfectly vertical stacking of the $Ni(CN)_2$ sheets and disorder in the orientation of the ligands around the z-axis, PICNIC structures will have tetragonal symmetry, a primitive cell with $a = b \sim 7.2$ Å, and intrinsic microporosity. Insofar as the network is not inherently rigid with respect to shear of the $Ni(CN)_2$ planes with respect to each other, PICNICs can be flexible in principle.

Culp et al. have synthesized over 40 distinct PICNIC structures using different ligands (18). Wong-Ng et al. determined the structure of several of these compounds (19). Of those which formed three-dimensional-type structures, all of them had lower symmetry than tetragonal and an in-plane periodic cell that was a supercell of an approximately 7.2 Å by 7.2 Å primitive cell, indicating ligand orientational ordering. Furthermore, various types of $CO_2$ gas adsorption isotherms are found (19). [The PICNIC-21 structure Ni-ByeMe shows a Type I isotherm (20), with $CO_2$ uptake at low pressure, and no hysteresis between $CO_2$ adsorption and desorption. The PICNIC-60 compound "Ni-Bpene" (Bpene = 1,2-bis(4-pyridyl)ethylene), on the other hand, shows little $CO_2$ uptake until a critical pressure is attained, and it also shows significant hysteresis in its adsorption-desorption plot (21-22). Studies of how the structure of PICNIC compounds depends on the ligand and how the structure in turn affects their gas adsorption properties will provide a useful basis for engineering PICNICs (and also MOFs) with desired gas adsorption properties.

In previous work (23), we used experimental measurements and density-functional-theory (DFT) calculations (24) to investigate in detail the structural changes in Ni-Bpene upon $CO_2$ adsorption. We concluded that rotations of the Bpene ligands occur as the structure goes from low $CO_2$ filling to maximum $CO_2$ uptake, along with a substantial expansion of the unit cell. In this work, we use density

functional theory calculations and analysis to elucidate how the local structure of adsorbent-free Ni-BpyMe differs from its average structure and the energetic reasons for its unusual structure.

**Methods**

We performed all calculations using the density functional theory code VASP (Refs. 25-26), version 5.4.1. [Certain commercial software is identified in this work in order to adequately specify the methodology used. Such identification does not imply recommendation or endorsement by the National Institute of Standards and Technology, nor does it imply that the software identified is necessarily the best available for the purpose.] The PAW_PBE pseudopotentials (27-28) C, H, N, and Ni_pv from the VASP 5.4 pseudopotential library were used for the corresponding elements. We used a plane-wave cutoff energy of 500 eV, and a Monkorst-Pack k-point grid corresponding to a 4x4x4 grid on a primitive PICNIC cell. The PBE exchange-correlation functional was used (29).

We found that the inclusion of dispersion interactions was essential to reproduce the structure of Ni-BpyMe. In Ref. (23), we found that the Hirshfeld form of dispersion with partial charges (30-33) worked very well for the structure of Ni-Bpene; thus, the same form of dispersion was used here. We used an isotropic Hubbard U correction (34) of 5 eV on Ni. As expected from crystal field splitting rules, Ni coordinated with 6 N are high-spin and the Ni coordinated with 4 C are low-spin. The energetics of magnetic ordering interactions were calculated be to less than $10^{-4}$ eV per high-spin Ni. We discovered that imposing antiferromagnetic ordering of the high-spin Ni would often cause undesired symmetry breaking of the parent crystallographic structure. We thus imposed ferromagnetic spin ordering on all structures studied, which ensures that the spin structures have the same symmetry as the crystallographic structures while having negligible effects on the energetics.

The experimental structural refinement of PICNIC-21 (Ref. 35) is shown in Figure 1 and the atomic coordinates listed in Table 1. Yellow atoms indicate sites with occupancy 0.5. The experimental structure refinement shows an average structure with strongly buckled $Ni(CN)_2$ planes and alternating *-z* and *+z* positioning of the methyl group for successive BpyMe ligands along the x direction. The methyl group orientation in the x-direction is disordered, which shows as 50% occupancy of this group in the structure refinement.

We began our studies of the structure of Ni-BpyMe by optimizing the structure of an isolated BpyMe molecule. Although the dihedral angle between the two pyridine rings in the BpyMe ligand in the average experimental structure of Ni-BpyMe is 90°, DFT optimization of an isolated BpyMe molecule gave a dihedral angle of 68°. We next investigated the idealized equilibrium structure for a BpyMe ligand in Ni-BpyMe. Based on known Ni-C and Ni-N bonding distances (35), we estimated that the equilibrium primitive cell for vertical BPyMe ligands is 7.20 Å by 7.20 Å by 11.27 Å. We fixed the unit cell at these dimensions, and relaxed the structure with one BPyMe ligand per unit cell. Figure 2 shows our definition for the orientational angle of the two pyridine rings of a BPyMe ligand in Ni-BpyMe. The equilibrium structure found for fixed cell dimensions has $\alpha$ = 15°, $\beta$ = 85° and thus a dihedral angle $\phi$ of 70°, slightly greater than that for the isolated BpyMe molecule. We initialized structures for DFT relaxation with BpyMe molecules with this dihedral angle. As the parent $Ni(CN)_2$ sheets have point group *4/mmm*, there are in principle 16 possible favorable BpyMe orientations. However, the point group is reduced to mmm for the experimental orthorhombic cell. Its crystal structure refinement has all methyl pyridine rings along the +/- *x* direction and the plain pyridine rings along the y direction. Thus

only 8 of the 16 theoretically favorable orientations of the ligand are relevant to the crystallography of this system. Our notation for the geometry of these 8 orientations is shown in Table 2.

Next, we generated an ensemble of BpyMe model orientational ordering patterns that are compatible with the experiment structure. Experimental disorder of the x direction of the methyl ring suggest that there are two possible orientations of each ligand. However, our modeling suggests that there are actually 4 possible orientations due to additional orientation disorder in the non-methyl ring. Each "up" ligand could be type 1, 2, 3 or 4 and each "down" ligand could be type 5, 6, 7, or 8.

In order to model crystallographic disorder, a supercell is required. For an exhaustive search of possible BpyMe orientations on a fixed supercell, the combinatorial explosion prevents using too large a supercell. In this work, we used a 1x2x2 supercell of the experimental cell, or a 2x2x2 supercell of the primitive PICNIC cell. This cell is sufficiently large to include all 8 orientations of the BpyMe ligand, while small enough for DFT calculations to be practical. At this size, there are $4^8 = 65536$ orientational orderings. By considering only structures with orthorhombic symmetry that contain methyl groups pointing in both the *+x* and *-x* directions, the number of symmetry-independent structures is reduced to 36. The configurations are labelled with an 8-digit code such as [58674132] that lists, in order, the orientations of the eight individual ligands whose centers are approximately at positions (0.25,0.25,0.25), (0.25,0.25,0.75), (0.25,0.75,0.25) etc. Incidentally, in each ensemble member included in this work, all BpyMe ligands were crystallographically equivalent. The structures were initialized with *flat* $Ni(CN)_2$ sheets.

We calculated the average crystallographic structure of the ensemble as follows. Let $i = 1,N_i$ label the symmetry-independent supercell configurations and $U_i$ their calculated energies. Let $j = 1,N_{Si}$ label a subset of point and translational symmetries of the primitive *Pmma* structure that generate all of the configurations symmetry-related to configuration i that are distinguishable by their 8-digit configuration codes. Let X be a coordinate of the crystal structure (lattice parameter, positional or occupancy). Local occupancy is defined as $P_{ij} = 1$ if the coordinate maps to a coordinate in the experimental structure refinement and $P_{ij} = 0$ otherwise. Then, for lattice parameter and positional coordinates, the ensemble average coordinate <X> is $\langle X \rangle = (\Sigma_{ij} P_{ij} X_{ij} \exp(-U_i/k_BT)) / (\Sigma_{ij} P_{ij} \exp(-U_i/k_BT))$, where $k_B$ is the Boltzmann constant and T the temperature. Ensemble average site occupancy coordinates are given by $\langle P \rangle = (\Sigma_{ij} P_{ij} \exp(-U_i/k_BT)) / (\Sigma_{ij} \exp(-U_i/k_BT))$. Note the factor $\exp(-U_i/k_BT)$ that creates a weighted Boltzmann distribution that is correct for the equilibrium ensemble in the limit of large supercells.

**Results and Discussion**

We first relaxed the structures with fixed 12.6025 Å by 2 x 7.3324 Å by 2 x 11.3095 Å unit cells matched to the experimental cell, and then allowed full relaxation. The average DFT structure, with and without unit cell relaxation are compared with experiment in table 3, and the fully relaxed average DFT structure is compared with experiment in Figure 3. The results for the structures are extremely similar to experiment, with a typical error in non-hydrogen atom position of less than 0.1 Å. The exception is the positions of the H atoms in the methyl group, where the DFT positions are rotated with respect to the positions reported in Ref. (35). We note, however, that experimental X-ray refinement does not actually provide all the H positions in this compound; some H positions were estimated (including the methyl hydrogens). Full relaxation shrinks lattice parameter *a*, expands *b* and *c*, and reduces the cell volume with respect to the experimental results. The fully relaxed configuration with the lowest energy,

configuration [58583232], is shown in Figure 4. The supercell periodicity is 2x1x2 that of a primitive PICNIC cell and 1x1x2 that of the experimental cell.

The deviation of the plain pyridine rings from the y-axis in Figure 4(b) are clear, but the methyl pyridine rings lie nearly along the x-axis. In terms of Figure 2, the angles are similar for both the fixed-cell and fully relaxed cell calculations: $\alpha$ is about 2°, $\beta$ is about 82°, and the dihedral angle $\phi$ is about 80°, compared with 68° for an isolated BpyMe molecule and 70° for BpyMe in the PICNIC reference cell. Ensemble averaging of ligands with different local orientation creates an average structure that has the plain pyridine ring exactly along the y-axis and the methyl pryridine ring exactly in the +/- *x* direction, and thus a dihedral angle of 90° for the average structure.

In both the experimental and DFT structure, the nominally flat $Ni(CN)_2$ are substantially buckled, with more than 2 Å peak to trough deviation in the height of the highest and lowest Ni positions. Rough conservation of bond lengths means that the *a/b* value is reduced from that for square $Ni(CN)_2$ layers. Keeping in mind that the *a* lattice parameter of Ni-BpyMe is double that for a primitive PICNIC cell, the ratio *a*/(2 *b*) is reduced from 1 for a square $Ni(CN)_2$ layer to 0.86 in the experimental structure to 0.83 in the fully relaxed DFT structure. This waviness is associated with alternate up and down positioning of the methyl group for successive ligands in the x direction.

Within the ensemble of structures for the fully-relaxed cell, there is a further hierarchy: those configurations containing pairs of BpyMe ligands along the x-direction that are oriented “face to toe” are all about 12 meV per ligand lower in energy than all of the configurations that contain “face to heel” orientation of successive ligands along the x-direction, thus dominating the Boltzmann ensemble. They are also about 2% lower in volume. This suggests that additional ligand ordering might be achieved experimentally if Ni-BpyMe were cooled to very low temperatures or put under pressure.

The calculated electronic density of states (DOS) for the lowest-energy configuration is shown in Figure 5, along with the approximate contribution of C, N, and Ni to the DOS. The PBE bandgap is about 3.1 eV. The experimental bandgap has not been reported. Normally, PBE calculations underestimate bandgaps, but the inclusion of the Hubbard U correction for Ni widens the gap between the highest occupied and lowest unoccupied Ni d-states, possibly bringing the bandgap closer to experiment. The highest occupied states are composed mainly of majority-spin Ni 3d electrons of the high-spin Ni and N 2p electrons from the neighboring Ni belonging to BpyMe ligands. The lowest unoccupied states are of either spin type, and are hybridized states fully involving the C and N framework of the BpyMe ligand. The slight gap between a narrow band of lowest unoccupied states and the continuum conduction band, along with the lack of Ni 3d contribution to this narrow band, suggest that these states are localized on individual BpyMe ligands.

We investigated how well DFT calculations would reproduce the BpyMe if the experimental cell distortion and ligand up-down ordering were not known. We repeated the ensemble calculations for a fixed large 2 x 7.20 Å by 2 x 7.20 Å by 2 x 11.27 Å reference PICNIC supercell. The ensemble was expanded to include orthorhombic configurations with mixed up and down type ligands in a given x-plane, yielding a total of 336 configurations. The results show a preference for face-to-heel ordering along the x-direction, but nothing favors the alternation of up and down orientations along x. This is a significant negative result: an exhaustive search of orientational ordering configurations at a fixed reference cell fails to find the actual orientational ordered pattern that is favored upon full relaxation.

The additional configurations were then added to experimental-cell ensemble. Now, all structures without up-down ligand alternation along x had energies at least 0.12 eV per ligand higher than all structures with this ordering. There is also a complete correspondence between a configuration having up-down ordering and having period-doubling waviness of the $Ni(CN)_2$ planes along the x direction.

To investigate the energetic origin of the structural distortion in Ni-BpyMe, we broke down the relaxational energy of the [58583232] configuration going from the larger reference cell to the fully relaxed cell, $\Delta U = U_{relax} - U_{large}$ as follows. The DFT calculations partition each calculated total energy $U_{total}$ into a PBE term and a dispersion term. The pure $Ni(CN)_2$ sheet contributions to the energy, $U_{sheet}$, are calculated by removing the ligands from the DFT structures and recomputing the energy (note that the N-coordinated Ni is now square planar coordinated, so it becomes low-spin). Pure ligand contributions to the energy $U_{ligand}$ are likewise computed by removing the $Ni(CN)_2$ planes. The ligand-plane interaction contributions to the total energy are simply given by $U_{ligand\text{-}sheet} = U_{total} - U_{sheet} - U_{ligand}$. The individual PBE and dispersion contributions to each term are determined in a similar manner.

The breakdown of the relaxation energetics is given in Table 4. The more favorable ligand-ligand interactions achieved by distorting the cell are counterbalanced by the energy penalty of buckling the sheets. The stability of the distorted structure is entirely due to improved ligand-sheet interactions. Furthermore, it is seen that the improvement in the ligand-sheet interactions is mainly due to more favorable dispersion interactions. Inspecting the crystal structure for van der Waals contact, it is clear that the significant dispersion interactions are between the methyl pyridine ring and the $Ni(CN)_2$ sheets. The following scenario applies. Strong dispersion interaction between methyl pyridine rings and the $Ni(CN)_2$ sheets causes the sheets to curve in the x-direction and the rings to orient roughly in this direction, in order to maximize contact. The curvature is balanced by opposite curvature "downstream", which doubles the cell and causes alternate methyl pyridine rings along the x direction to point up and down. A similar type of a cyanometallate plane distortion has been reported in pillared cadmium tetracyanonickelates (36), suggesting that strong ligand-cyanometallate dispersion interactions occur in other systems.

All DFT calculations in this work are effectively zero-temperature calculations. It would be interesting to include finite temperature effects via *ab initio* molecular dynamics or other methods to see to what degree the pyridine rings librate and the angular distribution of $\alpha$, $\beta$, and $\phi$ as a function of temperature.

In Figure 6, we compare the residual pores in the DFT structures for Ni-BPyMe with our earlier results for Ni-Bpene (23). We also calculated whether there was room for a $CO_2$ molecule to fit inside the pores in each case, using the minimal van der Waals radii tabulated in Ref. (37). In the case of Ni-BPyMe, the residual pores are large enough to allow $CO_2$ molecules to enter and move along the pores. For the Ni-Bpene structure, van der Waals collapse of the structure, leads to narrower tunnels insufficiently large to allow $CO_2$ to enter at low pressure, as is observed experimentally. Although the residual pores and Type-I adsorption isotherms of Ni-BpyMe could be taken as evidence that it is not flexible (35), it is clear that the volume can increase in principle by flattening the wavy $Ni(CN)_2$ planes. Indeed, with dimethyl-sulfonyl oxide inclusions, the volume per ligand is substantially larger than for empty Ni-BpyMe (19), indicating some capability of flexibility in the Ni-BpyMe system.

**Conclusions**

We have used a density-functional theory ensemble approach to explore the structure of the Hofmann-type compound Ni-BpyMe. The average structure agrees very well with experiment, but the local dihedral angle of the BpyMe ligand is different from its average value. The structural distortion in this system is driven by strong dispersion interactions between methyl pyridine rings and the $Ni(CN)_2$ sheets, and takes a form that leaves residual pore space in the empty structure. The development of a notation for configurational geometries, the observation that calculations on an undistorted reference cell may not give the right answer, and the discovery of a large dispersion interaction associated with a particular organic group are all things that can apply to other compounds in the "PICNIC" system and to metal-organic frameworks in general.

**Acknowledgements**

This technical effort was performed in support of the National Energy Technology's ongoing research in $CO_2$ capture under the RES contract DE-FE0004000. The authors gratefully acknowledge ChemMatCARS Sector 15 which is principally supported by the National Science Foundation/Department of Energy under grant number NSF/CHE-0822838. Figures 1, 3, and 4 were prepared using the VESTA visualization software (38). Figure 6 was prepared using the VMD software (39).

**References**

(1) Yaghi, O. M.; O'Keeffe, M.; Ockwig, N. W.; Chae, H. K.; Eddaoudi, M.; Kim, J. Reticular Synthesis and the Design of New Materials. Nature 2003, 423 (6941), 705–714. https://doi.org/10.1038/nature01650.

(2) James, S. L. Metal-Organic Frameworks. Chem. Soc. Rev. 2003, 32 (5), 276. https://doi.org/10.1039/b200393g.

(3) Kitagawa, S.; Kitaura, R.; Noro, S. Functional Porous Coordination Polymers. Angew. Chem. Int. Ed. 2004, 43 (18), 2334–2375. https://doi.org/10.1002/anie.200300610.

(4) Férey, G. Hybrid Porous Solids: Past, Present, Future. Chem. Soc. Rev. 2008, 37 (1), 191–214. https://doi.org/10.1039/b618320b.

(5) Furukawa, H.; Cordova, K. E.; O'Keeffe, M.; Yaghi, O. M. The Chemistry and Applications of Metal-Organic Frameworks. Science 2013, 341 (6149), 1230444. https://doi.org/10.1126/science.1230444.

(6) Eddaoudi, M. Systematic Design of Pore Size and Functionality in Isoreticular MOFs and Their Application in Methane Storage. Science 2002, 295 (5554), 469–472. https://doi.org/10.1126/science.1067208.

(7) Rosi, N. L. Hydrogen Storage in Microporous Metal-Organic Frameworks. Science 2003, 300 (5622), 1127–1129. https://doi.org/10.1126/science.1083440.

(8) Li, J.-R.; Kuppler, R. J.; Zhou, H.-C. Selective Gas Adsorption and Separation in Metal–Organic Frameworks. Chem. Soc. Rev. 2009, 38 (5), 1477. https://doi.org/10.1039/b802426j.

(9) Li, J.-R.; Sculley, J.; Zhou, H.-C. Metal–Organic Frameworks for Separations. Chem. Rev. 2011, 112 (2), 869–932. https://doi.org/10.1021/cr200190s.

(10) Sumida, K.; Rogow, D. L.; Mason, J. A.; McDonald, T. M.; Bloch, E. D.; Herm, Z. R.; Bae, T.-H.; Long, J. R. Carbon Dioxide Capture in Metal–Organic Frameworks. Chem. Rev. 2011, 112 (2), 724–781. https://doi.org/10.1021/cr2003272.

(11) Allendorf, M. D.; Houk, R. J. T.; Andruszkiewicz, L.; Talin, A. A.; Pikarsky, J.; Choudhury, A.; Gall, K. A.; Hesketh, P. J. Stress-Induced Chemical Detection Using Flexible Metal−Organic Frameworks. J. Am. Chem. Soc. 2008, 130 (44), 14404–14405. https://doi.org/10.1021/ja805235k.

(12) Férey, G.; Serre, C. Large Breathing Effects in Three-Dimensional Porous Hybrid Matter: Facts, Analyses, Rules and Consequences. Chem. Soc. Rev. 2009, 38 (5), 1380. https://doi.org/10.1039/b804302g.

(13) Alhamami, M.; Doan, H.; Cheng, C.-H. A Review on Breathing Behaviors of Metal-Organic-Frameworks (MOFs) for Gas Adsorption. Materials 2014, 7 (4), 3198–3250. https://doi.org/10.3390/ma7043198.

(14) Schneemann, A.; Bon, V.; Schwedler, I.; Senkovska, I.; Kaskel, S.; Fischer, R. A. Flexible Metal–Organic Frameworks. Chem. Soc. Rev. 2014, 43 (16), 6062–6096. https://doi.org/10.1039/c4cs00101j.

(15) Coudert, F.-X. Responsive Metal–Organic Frameworks and Framework Materials: Under Pressure, Taking the Heat, in the Spotlight, with Friends. Chem. Mater. 2015, 27 (6), 1905–1916. https://doi.org/10.1021/acs.chemmater.5b00046.

(16) Mellot-Draznieks, C.; Serre, C.; Surblé, S.; Audebrand, N.; Férey, G. Very Large Swelling in Hybrid Frameworks: A Combined Computational and Powder Diffraction Study. J. Am. Chem. Soc. 2005, 127 (46), 16273–16278. https://doi.org/10.1021/ja054900x.

(17) Cockayne, E. Thermodynamics of the Flexible Metal–Organic Framework Material MIL-53(Cr) From First-Principles. J. Phys. Chem. C 2017, 121 (8), 4312–4317. https://doi.org/10.1021/acs.jpcc.6b11692.

(18) Culp, J. T.; Madden, C.; Kauffman, K.; Shi, F.; Matranga, C. Screening Hofmann Compounds as CO2 Sorbents: Nontraditional Synthetic Route to Over 40 Different Pore-Functionalized and Flexible Pillared Cyanonickelates. Inorg. Chem. 2013, 52 (8), 4205–4216. https://doi.org/10.1021/ic301893p.

(19) Wong-Ng, W.; Culp, J.; Chen, Y.-S. Crystallography of Representative MOFs Based on Pillared Cyanonickelate (PICNIC) Architecture. Crystals 2016, 6 (9), 108. https://doi.org/10.3390/cryst6090108.

(20) Sing, K. S. W. Reporting Physisorption Data for Gas/Solid Systems with Special Reference to the Determination of Surface Area and Porosity (Recommendations 1984). Pure and Applied Chemistry 1985, 57 (4), 603–619. https://doi.org/10.1351/pac198557040603.

(21) Culp, J. T.; Smith, M. R.; Bittner, E.; Bockrath, B. Hysteresis in the Physisorption of CO2 and N2in a Flexible Pillared Layer Nickel Cyanide. J. Am. Chem. Soc. 2008, 130 (37), 12427–12434. https://doi.org/10.1021/ja802474b.

(22) Allen, A. J.; Espinal, L.; Wong-Ng, W.; Queen, W. L.; Brown, C. M.; Kline, S. R.; Kauffman, K. L.; Culp, J. T.; Matranga, C. Flexible Metal-Organic Framework Compounds: In Situ Studies for Selective CO2 Capture. Journal of Alloys and Compounds 2015, 647, 24–34. https://doi.org/10.1016/j.jallcom.2015.05.148.

(23) Allen, A.; Wong-Ng, W.; Cockayne, E.; Culp, J.; Matranga, C. Structural Basis of CO2 Adsorption in a Flexible Metal-Organic Framework Material. Nanomaterials 2019, 9 (3), 354. https://doi.org/10.3390/nano9030354.

(24) Cockayne, E. Contribution of Density Functional Theory to Microporous Materials for Carbon Capture. In Materials and Processes for CO2 Capture, Conversion, and Sequestration; John Wiley & Sons, Inc., 20418; pp 319–343. https://doi.org/10.1002/9781119231059.ch8.

(25) Kresse, G.; Furthmüller, J. Efficiency of Ab-Initio Total Energy Calculations for Metals and Semiconductors Using a Plane-Wave Basis Set. Computational Materials Science 1996, 6 (1), 15–50. https://doi.org/10.1016/0927-0256(96)00008-0.

(26) Kresse G., Furthmüller J. Efficient iterative schemes for ab initio total-energy calculations using a plane-wave basis set. Phys. Rev. B. 1996;54:11169–11186. doi: 10.1103/PhysRevB.54.11169.

(27) Blöchl, P. E. Projector Augmented-Wave Method. Phys. Rev. B 1994, 50 (24), 17953–17979. https://doi.org/10.1103/physrevb.50.17953.

(28) Kresse, G.; Joubert, D. From Ultrasoft Pseudopotentials to the Projector Augmented-Wave Method. Phys. Rev. B 1999, 59 (3), 1758–1775. https://doi.org/10.1103/physrevb.59.1758.

(29) Perdew, J. P.; Burke, K.; Ernzerhof, M. Generalized Gradient Approximation Made Simple. Phys. Rev. Lett. 1996, 77 (18), 3865–3868. https://doi.org/10.1103/physrevlett.77.3865.

(30) Bultinck, P.; Van Alsenoy, C.; Ayers, P. W.; Carbó-Dorca, R. Critical Analysis and Extension of the Hirshfeld Atoms in Molecules. The Journal of Chemical Physics 2007, 126 (14), 144111. https://doi.org/10.1063/1.2715563

(31) Kerber, T.; Sierka, M.; Sauer, J. Application of Semiempirical Long-Range Dispersion Corrections to Periodic Systems in Density Functional Theory. J. Comput. Chem. 2008, 29 (13), 2088–2097. https://doi.org/10.1002/jcc.21069.

(32) Bučko, T.; Lebègue, S.; Hafner, J.; Ángyán, J. G. Improved Density Dependent Correction for the Description of London Dispersion Forces. J. Chem. Theory Comput. 2013, 9 (10), 4293–4299. https://doi.org/10.1021/ct400694h.

(33) Bučko, T.; Lebègue, S.; Ángyán, J. G.; Hafner, J. Extending the Applicability of the Tkatchenko-Scheffler Dispersion Correction via Iterative Hirshfeld Partitioning. The Journal of Chemical Physics 2014, 141 (3), 034114. https://doi.org/10.1063/1.4890003.

(34) Liechtenstein, A. I.; Anisimov, V. I.; Zaanen, J. Density-Functional Theory and Strong Interactions: Orbital Ordering in Mott-Hubbard Insulators. Phys. Rev. B 1995, 52 (8), R5467–R5470. https://doi.org/10.1103/physrevb.52.r5467.

(35) Wong-Ng, W.; Culp, J.; Siderius, D. W.; Chen, Y.; Wang, S. Y. G.; Allen, A. J.; Cockayne, E. Synthesis, Structural and Sorption Characterization of a Hofmann Compound, Ni(3-Methy-4,4'-Bipyridine)[Ni(CN)4]. Polyhedron 2021, 200, 115132. https://doi.org/10.1016/j.poly.2021.115132.

(36) Nishikiori, S.; Iwamoto, T. Crystal Structures of (.Alpha.,.Omega.-Diaminoalkane)Cadmium(II) Tetracyanonickelate(II)-Aromatic Molecule Inclusion Compounds. 3. (1,4-Diaminobutane)Cadmium(II) Tetracyanonickelate(II)-Pyrrole (1/1), (1,4-Diaminobutane)Cadmium(II) Tetracyanonickelate(II)-Aniline (2/3), and (1,4-Diaminobutane)Cadmium(II) Tetracyanonickelate(II)-N,N-Dimethylaniline (1/1). Inorg. Chem. 1986, 25 (6), 788–794. https://doi.org/10.1021/ic00226a013.

(37) Batsanov, S. S. Van der Waals Radii of Elements. Inorganic Materials 2001, 37, 871-885. https://doi.org/10.1023/a:1011625728803.

(38) Momma, K.; Izumi, F. VESTA: A Three-Dimensional Visualization System for Electronic and Structural Analysis. J Appl Cryst 2008, 41 (3), 653–658. https://doi.org/10.1107/s0021889808012016.

(39) Humphrey, W.; Dalke, A.; Schulten, K. VMD: Visual Molecular Dynamics. Journal of Molecular Graphics 1996, 14 (1), 33–38. https://doi.org/10.1016/0263-7855(96)00018-5.

**Tables**

Table 1 Experimental atomic coordinates for Ni-BpyMe (Ref. 35). Space group *Pmma*. Lattice parameters a = 12.6025(4) Å, b = 7.3324(3) Å, c = 11.3095(4) Å

| Site | x | y | z | Wyckoff position | Occupancy |
|---|---|---|---|---|---|
| C(1) | 0.8408(2) | 0.5 | 0.8577(2) | 4j | 1 |
| C(2) | 0.8450(2) | 0.5 | 0.7351(2) | 4j | 1 |
| C(3) | 0.75 | 0.5 | 0.6717(3) | 2f | 1 |
| C(4) | 0.75 | 0.5 | 0.5410(3) | 2f | 1 |
| C(5) | 0.75 | 0.6584(5) | 0.4770(3) | 4k | 1 |
| C(6) | 0.75 | 0.6542(4) | 0.3537(3) | 4k | 1 |
| C(7) | 0.9520(7) | 0.5 | 0.6767(7) | 4j | 0.5 |
| C(9) | 0.5832(1) | 0.1811(2) | 0.0683(2) | 8ℓ | 1 |
| N(1) | 0.75 | 0.5 | 0.2931(2) | 2f | 1 |
| N(2) | 0.75 | 0.5 | 0.9183(3) | 2f | 1 |
| N(8) | 0.6363(1) | 0.2974(2) | 0.1019(1) | 8ℓ | 1 |
| Ni(1) | 0.75 | 0.5 | 0.1073(1) | 2f | 1 |
| Ni(2) | 0.5 | 0. | 0. | 2a | 1 |
| H(1) | 0.9056 | 0.5 | 0.9004 | 4j | 1 |
| H(2) | 0.9144 | 0.5 | 0.6981 | 4j | 0.5 |
| H(5) | 0.75 | 0.7724 | 0.5170 | 4k | 1 |
| H(6) | 0.75 | 0.7664 | 0.3117 | 4k | 1 |
| H(7A) | 0.9410 | 0.5 | 0.5926 | 4j | 0.5 |
| H(7B) | 0.9915 | 0.6069 | 0.6991 | 8ℓ | 0.5 |

Table 2. Notation for NBpyMe ligand orientations used in initializing the configurations explored in this work. The angles $\alpha$ and $\beta$ refer to Figure 2.

| Notation | $\alpha$ | $\beta$ | Methyl z | Notation | $\alpha$ | $\beta$ | Methyl z |
|---|---|---|---|---|---|---|---|
| 1 | 9° | 82° | up | 5 | 9° | 82° | down |
| 2 | -9° | -82° | up | 6 | -9° | -82° | down |
| 3 | 171° | 98° | up | 7 | 171° | 98° | down |
| 4 | -171° | -98° | up | 8 | -171° | -98° | down |

Table 3 Comparison of experimental and symmetry-and-ensemble averaged DFT structures of Ni-BpyMe. Site notation, partial occupancies, and Wyckoff positions are as in Table 1. Coordinates that are fixed by symmetry are not shown. Large differences in the H(7A) and H(7B) coordinates between experiment and DFT are due to the rotation of the methyl group in the DFT relaxations.

| | Expt. | DFT fixed cell | DFT full relaxation | | Expt. | DFT fixed cell | DFT full relaxation |
|---|---|---|---|---|---|---|---|
| *a* (Å) | 12.6025 | 12.6025 | 12.2661 | N(8)x | 0.6363 | 0.6353 | 0.6329 |
| *b* (Å) | 7.3324 | 7.3324 | 7.3739 | N(8)y | 0.2974 | 0.2968 | 0.2971 |
| *c* (Å) | 11.3095 | 11.3095 | 11.3661 | N(8)z | 0.1019 | 0.1070 | 0.1130 |
| *V* (Å$^3$) | 1045.07 | 1045.07 | 1027.60 | Ni(1)z | 0.1073 | 0.1112 | 0.1178 |
| C(1)x | 0.8408 | 0.8415 | 0.8438 | H(1)x | 0.9056 | 0.9140 | 0.9229 |
| C(1)z | 0.8577 | 0.8610 | 0.8666 | H(1)z | 0.9004 | 0.9120 | 0.9126 |
| C(2)x | 0.8450 | 0.8460 | 0.8484 | H(2)x | 0.9144 | 0.9283 | 0.9284 |
| C(2)z | 0.7351 | 0.7380 | 0.7441 | H(2)z | 0.6981 | 0.6973 | 0.7103 |
| C(3)z | 0.6717 | 0.6752 | 0.6815 | H(5)y | 0.7724 | 0.7914 | 0.7884 |
| C(4)z | 0.5410 | 0.5442 | 0.5511 | H(5)z | 0.5170 | 0.5264 | 0.5329 |
| C(5)y | 0.6584 | 0.6621 | 0.6602 | H(6)y | 0.7663 | 0.7786 | 0.7759 |
| C(5)z | 0.4770 | 0.4803 | 0.4873 | H(6)z | 0.3117 | 0.3038 | 0.3118 |
| C(6)y | 0.6542 | 0.6562 | 0.6545 | H(7A)x | 0.9410 | 1.0114 | 1.0242 |
| C(6)z | 0.3537 | 0.3575 | 0.3651 | H(7A)z | 0.5926 | 0.7351 | 0.7318 |
| C(7)x | 0.9520 | 0.9460 | 0.9554 | H(7B)x | 0.9914 | 0.9547 | 0.9626 |
| C(7)z | 0.6767 | 0.6723 | 0.6716 | H(7B)y | 0.6069 | 0.6192 | 0.6187 |
| C(9)x | 0.5832 | 0.5804 | 0.5822 | H(7B)z | 0.6991 | 0.6157 | 0.6148 |
| C(9)y | 0.1811 | 0.1795 | 0.1794 | | | | |
| C(9)z | 0.0683 | 0.0698 | 0.0746 | Local $\alpha$ | | 2.1 | 1.5 |
| N(1)z | 0.2931 | 0.2972 | 0.3047 | Local $\beta$ | | 83.0 | 81.4 |
| N(2)z | 0.9183 | 0.9215 | 0.9270 | Local $\phi$ | | 80.9 | 79.9 |

Table 4. Calculated contributions to energy change in going from large reference cell with nearly flat $Ni(CN)_2$ sheets to fully relaxed cell with wavy $Ni(CN)_2$ sheets. Units are eV per ligand.

| | Total | PBE ("Chemical") | Dispersion |
|---|---|---|---|
| Total | -0.263 | +0.048 | -0.311 |
| sheet | +0.163 | +0.179 | -0.016 |
| ligand | -0.152 | -0.074 | -0.078 |
| ligand-sheet | -0.274 | -0.057 | -0.217 |

**Figures**

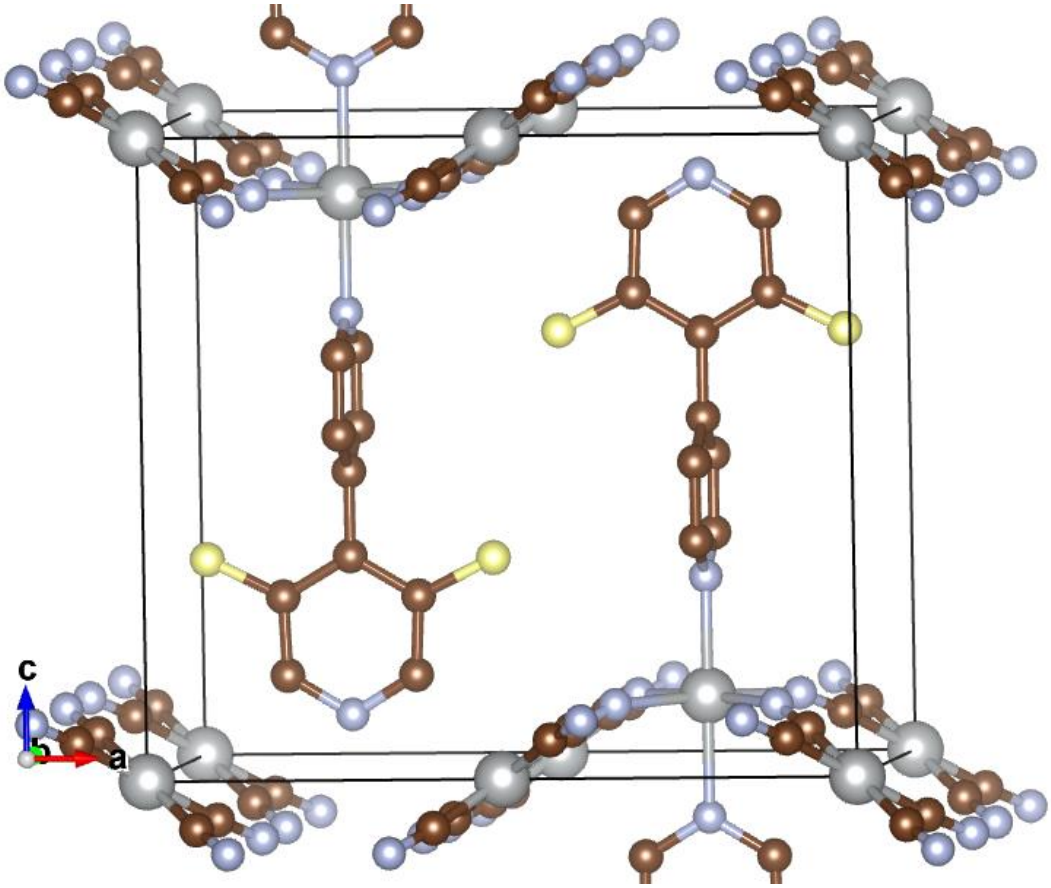


Figure 1. Structure of Ni-BpyMe, as determined from X-ray diffraction refinement. Ni atoms are gray, C brown, and N blue. Hydrogen are not shown for clarity. Yellow sites are carbon positions with 0.5 occupancy, indicating that the methyl group of an individual ligand points either in the +*x* or the -*x* direction.

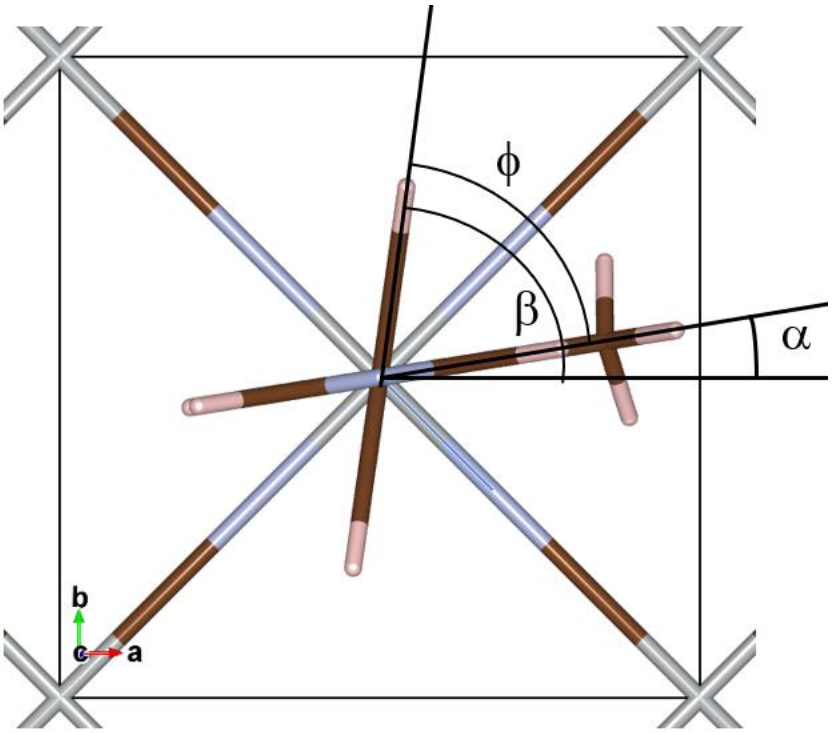


Figure 2. Definition of the orientation of the methyl pyridine (a) and plain pyridine ring (b) of a NiByMe in Ni-BpyMe. The dihedral angle $\phi$ is $|\beta - \alpha|$. Note that $\beta$ is only defined modulo 180°.

(a)

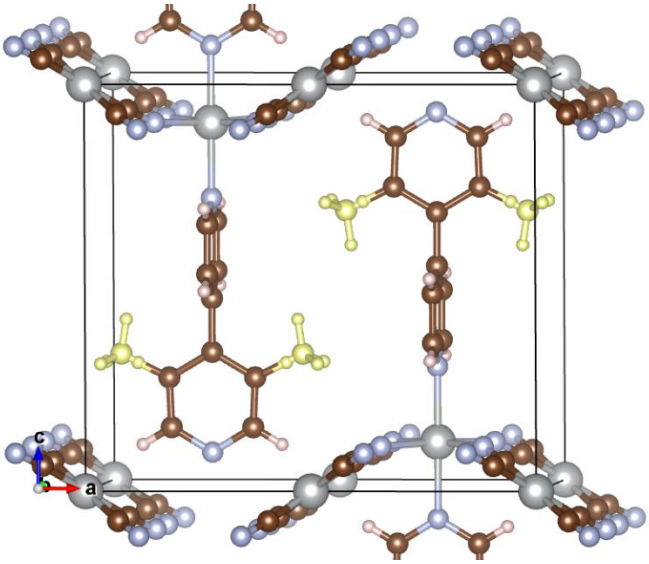


(b)

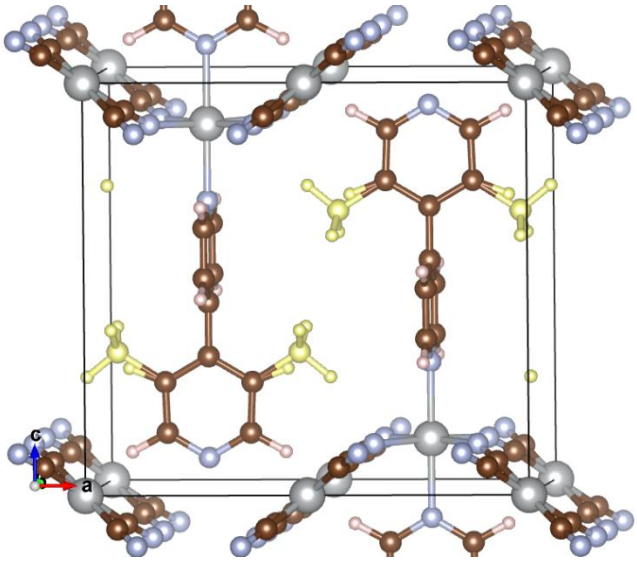


Figure 3. Comparison of (a) experimental (35) and (b) DFT structures of Ni-BpyMe. Coloring is the same as in Figure 1, except H atoms are small pink. Sites of partial occupancy 0.5 are shown in yellow; larger = C; smaller = H. Note the rotation of methyl group hydrogen positions in the DFT structure compared with those reported in Ref. (35).

(a)

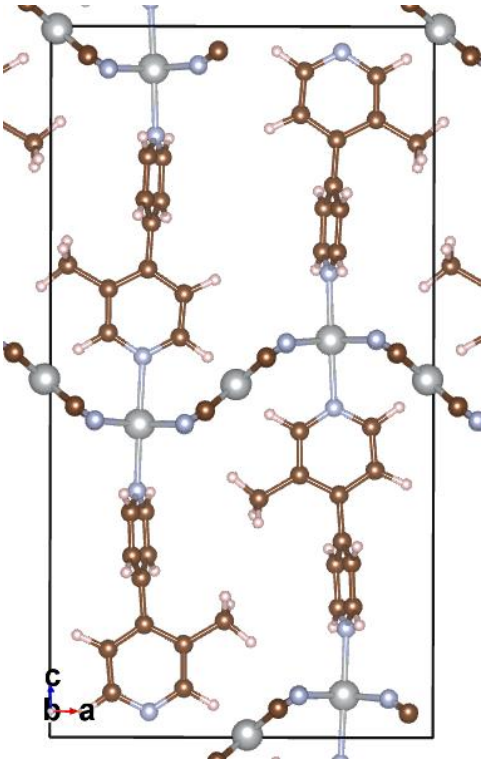


(b)

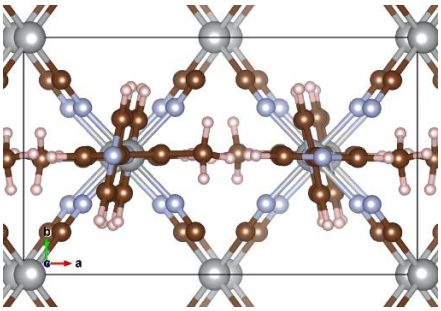


Figure 4. Views of the single lowest-energy DFT ordered configuration of Ni-BpyMe (a) up the y-axis; (b) down the z-axis.

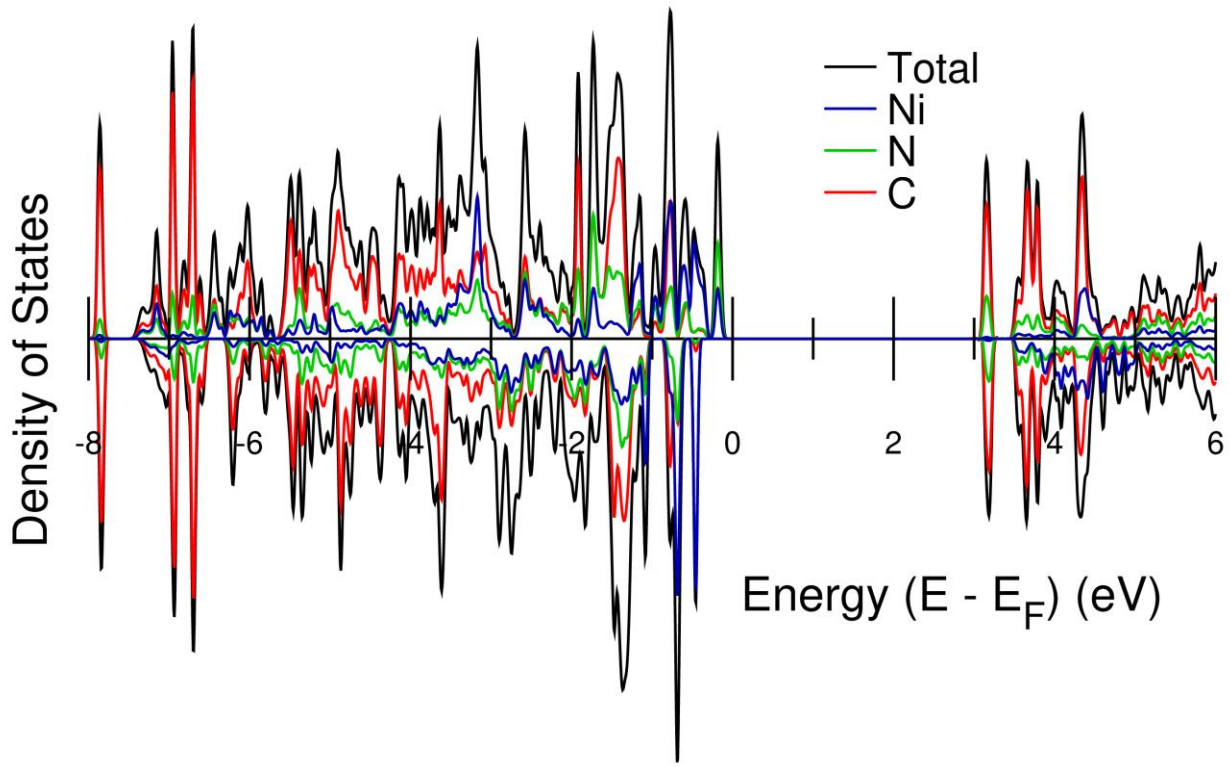


Figure 5. Calculated density of states (DOS) for the lowest-energy Ni-BpyMe structure found. The majority-spin DOS is above the line and minority-spin DOS below. The approximate relative contributions of Ni, N, and C electrons to the DOS are also shown. The contribution of H is small and is not shown.

(a)

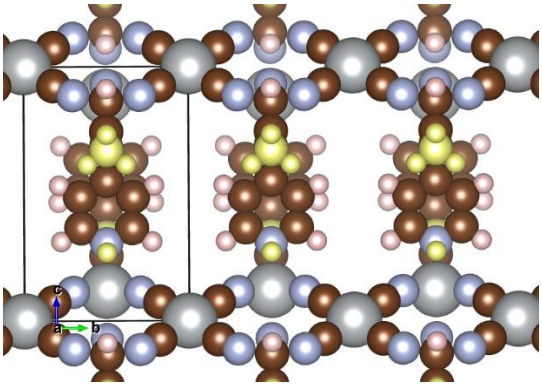


(b)

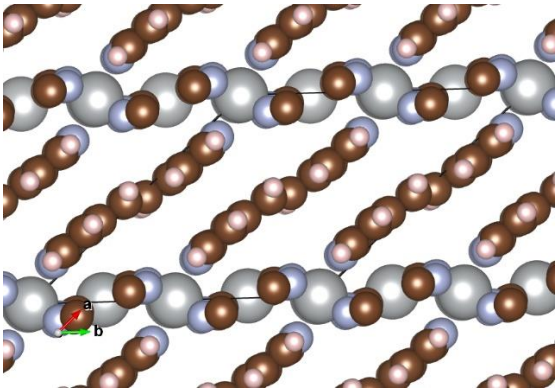


Figure 6. Comparative DFT empty structures of (a) Ni-BpyMe and (b) Ni-Bpene. Atoms are drawn with their van der Waals radii shown. The large pores in (a) should allow gas species to adsorb more readily at low pressures, as is confirmed for the case of $CO_2$ via detailed van der Waals calculations.

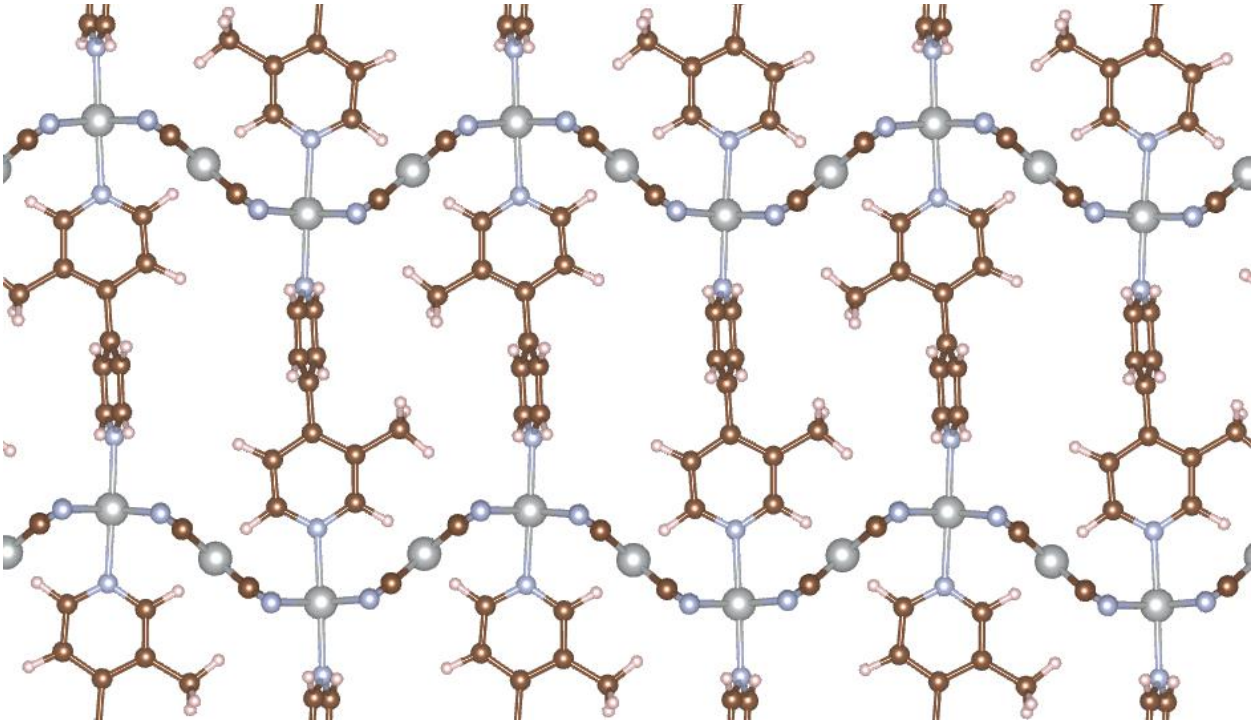

TOC Graphic